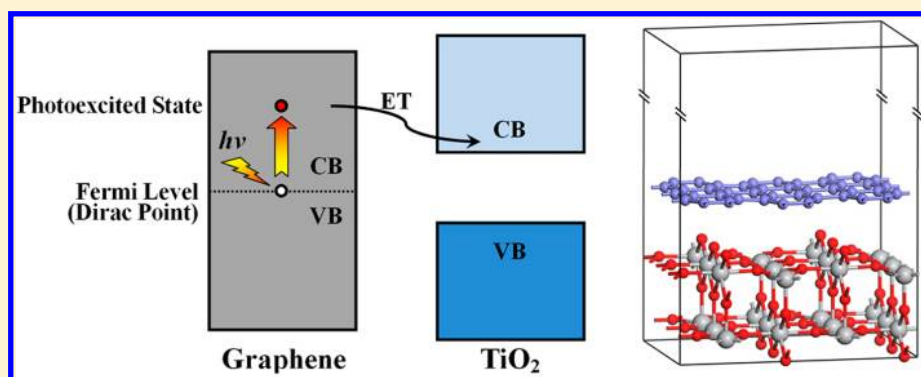# Photo-induced Charge Separation across the Graphene–TiO₂ Interface Is Faster than Energy Losses: A Time-Domain *ab Initio* Analysis

Run Long,[†,‡,§] Niall J. English,[§] and Oleg V. Prezhdo*[,†]

[†]Department of Chemistry, University of Rochester, New York 14620, United States

[‡]Complex & Adaptive Systems Laboratory, School of Physics, University College Dublin, Belfield, Dublin 4, Ireland

[§]The SEC Research Cluster, School of Chemical & Bioprocess Engineering, University College Dublin, Belfield, Dublin 4, Ireland

ABSTRACT: Graphene–TiO₂ composites exhibit excellent potential for photovoltaic applications, provided that efficient photoinduced charge separation can be achieved at the interface. Once charges are separated, TiO₂ acts as an electron carrier, while graphene is an excellent hole conductor. However, charge separation competes with energy losses that can result in rapid electron–hole annihilation inside metallic graphene. Bearing this in mind, we investigate the mechanisms and, crucially, time scales of electron transfer and energy relaxation processes. Using nonadiabatic molecular dynamics formulated within the framework of time-domain density functional theory, we establish that the photoinduced electron transfer occurs several times faster than the electron–phonon energy relaxation (i.e., charge separation is efficient in the presence of electron–phonon relaxation), thereby showing that graphene–TiO₂ interfaces can form the basis for photovoltaic and photocatalytic devices using visible light. We identify the mechanisms for charge separation and energy losses, both of which proceed by rapid, phonon-induced nonadiabatic transitions within the manifold of the electronic states. Electron injection is ultrafast, owing to strong electronic coupling between graphene and TiO₂. Injection is promoted by both out-of-plane graphene motions, which modulate the graphene–TiO₂ distance and interaction, and high-frequency bond stretching and bending vibrations, which generate large nonadiabatic coupling. Both electron injection and energy transfer, injection in particular, accelerate for photoexcited states that are delocalized between the two subsystems. The theoretical results show excellent agreement with the available experimental data [*Adv. Funct. Mater.* **2009**, *19*, 3638]. The state-of-the-art simulation generates a detailed time-domain atomistic description of the interfacial charge separation and relaxation processes that are fundamental to a wide variety of applications, including catalysis, electrolysis, and photovoltaics.

1. INTRODUCTION

Sunlight provides an enormous source of energy that can be harvested in a variety of ways. Examples include conversion of solar energy into electricity and chemical energy, for instance by water splitting and generation of hydrogen fuel, photo-degradation of environmentally hazardous compounds (organic, inorganic, and biological pollutants), photochemical catalysis, and photosynthesis. These and other light-induced processes have received intense attention during the past decade.[1−7] In the vast majority of cases, photoinduced electron transfer (ET) at an interface of two materials with a chemical potential difference has received particular scrutiny because it is a key process in solar energy systems and photocatalysis.

Among the broad spectrum of materials used for light harvesting and utilization, titanium dioxide (TiO₂) has established itself as one of the most widely used inorganic semiconductors. TiO₂ exhibits excellent physical and chemical stability, is nontoxic, possesses desirable electronic and optical properties, and has low cost. As a wide band gap semiconductor, with light absorption at about 3.20 and 3.05 eV for anatase and rutile polymorphs, respectively, TiO₂ can be used directly only with ultraviolet light. Narrowing the band gap to the visible range provides a straightforward way for achieving

higher photovoltaic and photocatalytic activity, because light absorption and the consequent photoexcitation of electron—hole pairs occur when the energy of the incident photons matches or exceeds the band gap. Realization of semiconductor band gaps in the visible region (ca. 2.3–2.6 eV) leads to harvesting longer solar-radiation wavelengths and, all other factors being equal, generating greater fluxes of photoexcited (PE) electrons. PE electrons can either be channeled to create electricity directly in photovoltaic solar cells or else be used to drive chemical reactions. Doping with impurity atoms is a reasonably effective way to narrow the band gap. However, the large energy required for introduction of dopant atoms into the TiO_2 lattice restricts sample synthesis. Dopant-mediated electron—hole recombination in the lattice can be a significant postexcitation problem restricting practical realization. As a potentially attractive alternative approach, composites of TiO_2 with other materials can help to overcome these shortcomings. Examples include molecular chromophores,[8] conjugated polymers,[9] semiconductor quantum dots,[10,11] and nanoscale carbon materials.[12–14] TiO_2 and the above-mentioned complementary components often possess very different properties, for example, localized vs. delocalized electronic states, high- vs. low-frequency vibrational modes, soft organic vs. hard inorganic materials, good vs. poor conductors of electricity and heat, well-ordered vs. disordered phases, and so on. An additional layer of complexity in the design and performance analysis of such composite systems arises due to interfacial interactions and experimental uncertainties, such as TiO_2 surface roughness, the presence of defects, the effect of organic solvents, local electrolyte concentration, charge build-up, etc.

Recently, composites of TiO_2 with nanoscale carbon materials have attracted significant attention. Many experimental efforts are currently focusing on the synthesis of hybrid graphene—TiO_2 nanocomposites,[15–18] demonstrating high stability and enhanced photovoltaic properties. The unique electronic structure of graphene has led to many applications in solar cells.[19–22] Graphene's advantages include high surface area (theoretical value of 2630 m²/g)[23] for improved interfacial contact, excellent electronic conductivity, and outstanding mechanical properties.[24,25] The hybrid graphene—TiO_2 materials display activity under visible-light irradiation and harvest a larger fraction of the solar spectrum vis-à-vis many other nanostructured materials; therefore, photoinduced electron—hole pairs may be created relatively readily by photon absorption. PE electrons can then produce electricity[19–22] or drive a water-splitting reaction to generate hydrogen.[26] However, since graphene is a metal, photoinduced electrons and holes may suffer rapid electron—vibrational relaxation and recombination,[27,28] greatly decreasing the efficiencies of photovoltaic and photocatalytic devices. The competition between the photoinduced ET and the electron—vibrational energy relaxation determines directly the solar power conversion efficiencies. Recently, Manga et al. reported that ultrafast ET occurs within 200 fs in hybrid graphene—titania materials and that this achieves efficient photocurrent conversion.[17] These experimental findings provide strong motivation for the development of graphene—TiO_2 solar cells. The extremely fast, 0.2 ps, time scale for ET from the graphene sheet into the TiO_2 surface[17] makes it difficult to invoke Marcus theory, which requires slow ET dynamics to allow for redistribution of vibrational energy.

The dye-sensitized semiconductor solar cell (DSSC) presents a classic example of a photovoltaic device based on

TiO_2.[29] The charge separation at the chromophore—inorganic semiconductor interface has been investigated in many experimental and theoretical studies.[30–42] An understanding of the ET mechanisms generates valuable and, often, critical insights into photoinduced electron dynamics and provides guidelines for system design and improvement. The injection rate has been found to depend heavily on the electronic properties of the dye and the semiconductor, as well as on the distance between them, as characterized by the length and chemical composition of the molecular bridge. Competing ET mechanisms have been proposed to explain the observed ultrafast injection events,[34,38] having substantially different implications for the variation of the interface conductance and solar cell voltage with system properties. To date, direct simulation of ET at interfaces composed of two dissimilar materials has been very challenging. In the previous studies, we have characterized photoinduced ET at molecule—TiO_2 interfaces[43–46] using real-time nonadiabatic molecular dynamics (NAMD) implemented within the time-dependent density functional theory (TD-DFT) framework.[47–49] Subsequently, the method has been applied to the more complex interfaces of TiO_2 with a water layer[50] and with a semiconductor quantum dot.[51] These studies have led to an understanding of the mechanisms of ET, relaxation, and recombination dynamics, and the effect of these processes on the solar cell efficiencies.

In view of the central importance of TiO_2 and graphene for applications as photocatalysts and solar energy materials, the current study focuses on the photoinduced electron—vibrational dynamics at the graphene—TiO_2 interface. Figure 1
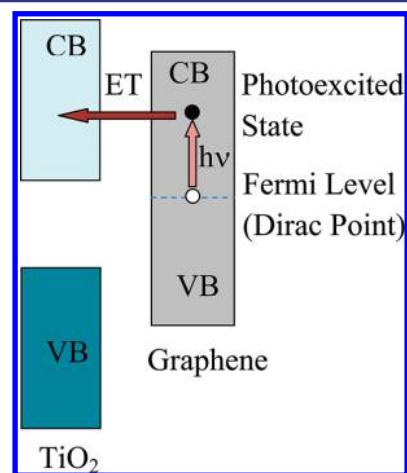
Figure 1. Schematic of the photoinduced electron injection process. An absorbed photon promotes an electron from the graphene Fermi energy located in the TiO_2 band gap into an excited state that is in resonance with the TiO_2 conduction band. The excited electron is injected into TiO_2, simultaneously relaxing in energy by coupling to vibrations.

depicts the diagram of the energy levels at the interface. An absorbed photon promotes an electron from the graphene ground state, located within the TiO_2 energy gap, to an excited state that is in resonance with the TiO_2 conduction band (CB). The hot electron moves from graphene into TiO_2, simultaneously losing energy to atomic vibrations. The energy deposited into vibrational modes of graphene is transferred into TiO_2 vibrational modes. The nature of the PE state, as well as the competition between the ET, energy transfer, and energy

relaxation constitute the subject of the current time-domain *ab initio* simulation.

The next section describes the essential theoretical background and computational details of the simulation. The Results and Discussion section starts with a discussion of the geometric and electronic structure of the graphene–TiO_2 system, followed by an analysis of the nuclear dynamics and electron-vibrational coupling. A detailed examination on the ET, energy relaxation, and energy transfer processes is presented next. The simulation results are compared with available experimental data. The article concludes with a summary of the most important findings.

2. THEORETICAL METHODOLOGY

The NAMD simulation of electron relaxation dynamics is carried out using the mixed quantum–classical approach[47,48] implementing the fewest switching surface hopping (FSSH) technique[52–54] within TD-DFT[55–57] in the Kohn–Sham (KS) representation.[58] The electrons are treated quantum mechanically, while the nuclei, which are much heavier and slower, are treated classically. Details of this approach can be found in ref 59, and here we outline the procedure briefly.

2.1. Time-Dependent Kohn–Sham Theory for Electron–Nuclear Dynamics. NA effects may be incorporated into ET dynamics by TD-DFT[55–57] within the KS framework,[58] where the electron density, $\rho(\mathbf{r},t)$, is expressed by the sum of the densities of the occupied single-electron KS orbitals, $\varphi_p(\mathbf{r},t)$:

$$\rho(\mathbf{r}, t) = \sum_{n=1}^{N_e} |\varphi_p(\mathbf{r}, t)|^2 \tag{1}$$

The evolution of the electron density is determined by the TD variational principle applied to the KS energy:

$$E\{\varphi_p\} = \sum_{p=1}^{N_e} \left\langle \varphi_p|K|\varphi_p \right\rangle + \sum_{p=1}^{N_e} \left\langle \varphi_p|V|\varphi_p \right\rangle + \frac{e^2}{2} \iint \frac{\rho(\mathbf{r}', t)\rho(\mathbf{r}, t)}{|\mathbf{r} - \mathbf{r}'|}$$
$$d^3\mathbf{r}\, d^3\mathbf{r}' + E_{XC}\{\rho\} \tag{2}$$

where the first, second, third, and fourth term on the right-hand side represent the electron kinetic energy, the electron–nuclear attraction, the electron–electron Coulomb repulsion, and the exchange–correlation energy functional, respectively. The TD variational principle gives a set of single-particle equations for the evolution of the KS orbitals[58,60]

$$i\hbar \frac{\partial \varphi_p(\mathbf{r}, t)}{\partial t} = H(\mathbf{r}, \mathbf{R}, t)\varphi_p(\mathbf{r}, t) \tag{3}$$

where $p = 1, 2, ..., N_e$, and N_e is the number of electrons. These single-electron equations are coupled because the Hamiltonian, H, known as the density functional, depends on the overall electron density. The electron–vibrational coupling enters the Hamiltonian through the external potential created by the atoms.

The single-electron orbitals in eq 3 are expressed in the adiabatic KS basis $\tilde{\varphi}_p(\mathbf{r},\mathbf{R}(t))$, which is calculated for the current atomic positions $\mathbf{R}$. The adiabatic representation of the PE electron orbital is shown in eq 4.

$$\varphi_{PE}(\mathbf{r}, t) = \sum_k c_k(t)\tilde{\varphi}_k(\mathbf{r}; \mathbf{R}(t)) \tag{4}$$

By inserting this into eq 3, we obtain the equation describing the evolution of the expansion coefficients:

$$i\hbar \frac{\partial}{\partial t} c_j(t) = \sum_k c_k(t)(\varepsilon_k \delta_{jk} + d_{jk}) \tag{5}$$

where ε_k is the energy of the adiabatic state k, and d_{jk} represents the NA coupling between orbitals k and j. The latter is generated by

atomic motions. We calculate the NA coupling d_{jk} numerically as the overlap of orbitals j and k at sequential time steps[53]

$$d_{jk} = -i\hbar \left\langle \tilde{\varphi}_j|\nabla_R|\tilde{\varphi}_k \right\rangle \cdot \frac{d\mathbf{R}}{dt} = -i\hbar \left\langle \tilde{\varphi}_j|\frac{\partial}{\partial t}|\tilde{\varphi}_k \right\rangle$$
$$\approx -\frac{i\hbar}{2\Delta t}(\left\langle \tilde{\varphi}_j(t)|\tilde{\varphi}_k(t + \Delta t) \right\rangle - \left\langle \tilde{\varphi}_j(t + \Delta t)|\tilde{\varphi}_k(t) \right\rangle) \tag{6}$$

2.2. Electron Transfer Mechanisms. The photoinduced ET can proceed by several mechanisms, Figure 2, and our simulation allows us
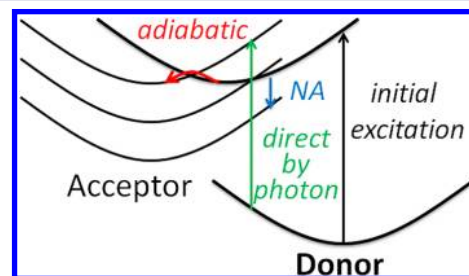
Figure 2. Mechanisms of the photoinduced electron transfer. The photoexcited donor can transfer the electron to the acceptor adiabatically by passing over a transition state barrier (curved red arrow). Alternatively, the transfer can occur nonadiabatically, via a hop between donor and acceptor states away from the transition state (downward blue arrow). In the case of strong donor–acceptor coupling, photoexcitation can promote the electron directly from the donor ground state to an acceptor excited state (upward green arrow).

to distinguish among them. In the case of a strong electronic donor–acceptor coupling, the PE state can contain a significant contribution from the acceptor species. ET to the acceptor during the optical excitation constitutes the direct ET mechanism. By defining the PE state as an eigenstate of the electronic subsystem with a large optical transition dipole moment, we model system interaction with a continuous wave light, representative of solar radiation. The fraction of the PE state density localized on TiO_2 characterizes the contribution of the direct mechanism to the overall ET process.

Even with an extremely strong donor–acceptor coupling, a significant fraction of the PE state density is localized on the graphene donor. This is because the ground state resides within the TiO_2 band gap and is fully localized on graphene, Figure 1, while optical selection rules require overlap between the ground and excited states. Transfer of the PE electron localized on the donor into the acceptor can proceed by either an adiabatic or a NA mechanism, Figure 2. During adiabatic transfer, the system remains in the same electronic state, but the state localization changes from the donor to the acceptor as a result of an atomic motion along the reaction coordinate. NA transfer involves transitions between electronic states. It becomes more important when the donor–acceptor coupling is weak.

The extent of ET from graphene to the TiO_2 surface is computed by integrating the PE electron density over the region of the simulation cell occupied by the graphene sheet, Figures 3 and 4.

$$\int_{graphene} \rho_{PE}(\mathbf{r}, t)\, d\mathbf{r} = \int_{graphene} |\varphi_{PE}(\mathbf{r}, t)|^2\, d\mathbf{r}$$
$$= \sum_{k,j} c_k^*(t)c_j(t) \int_{graphene} \tilde{\varphi}_k^*(\mathbf{r}, \mathbf{R}(t))\tilde{\varphi}_j$$
$$(\mathbf{r}, \mathbf{R}(t))\, d\mathbf{r} \tag{7}$$

The time derivative of eq 7 gives expressions for the adiabatic and NA contributions to ET:
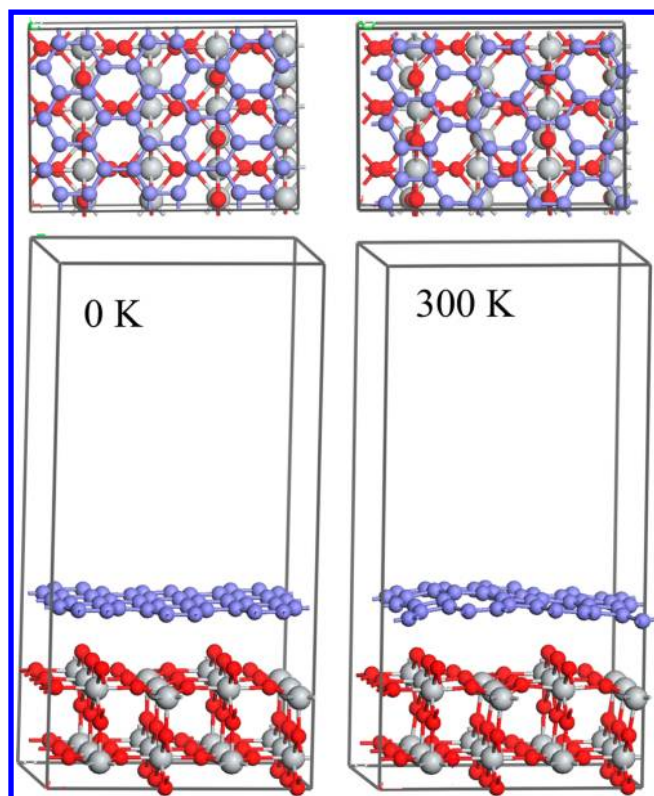
Figure 3. Top and side views of the simulation cell showing the geometry of the hybrid graphene–TiO$_2$ system optimized at 0 K (left) and during the molecular dynamics at 300 K (right). Rearrangement of some of the six-atom carbon rings into four- and eight-atom rings, as well as notable out-of-plane fluctuations of graphene, affect its electronic structure and increase the graphene–TiO$_2$ coupling at room temperature.

$$\frac{d \int_{graphene} \rho_{PE}(\mathbf{r}, t)\, d\mathbf{r}}{dt}$$

$$= \sum_{k,j} \left\{ \frac{d(c_i^* c_j)}{dt} \int_{graphene} \phi_i^* \phi_j\, d\mathbf{r} + c_i^* c_j \frac{d \int_{graphene} \phi_i^* \phi_j\, d\mathbf{r}}{dt} \right\}$$

$$(8)$$

The first term has fixed localizations of adiabatic states but changing occupations, while the second term has fixed adiabatic state occupations but changing localizations. These terms correspond to NA ET and adiabatic ET, respectively. Note that even adiabatic ET can and does involve NA dynamics. To be transferred, the PE electron in the graphene state has to find a strongly coupled TiO$_2$ state by hopping over several uncoupled TiO$_2$ CB states. The above definition of the NA ET mechanism includes this factor by considering only those NA transitions that produce the overall shift of the electron density from graphene into TiO$_2$.

The ET mechanisms carry different implications for the variation of the interface conductance and solar cell voltage with system properties. Direct ET indicates that the interface cannot be viewed as a simple sum of the two components. A qualitatively new electronic state, shared by the donor and the acceptor, is created due to the strong donor–acceptor coupling. The state is essential for electron transport across the interface. Direct electron injection implies that positive and negative charges are created at the energy of the absorbed photon. This fact can be used to avoid energy and voltage losses to heat. Adiabatic ET also requires strong donor–acceptor interaction. In addition, it needs an energy fluctuation that can bring the system across the transition state. A fast exchange of energy between vibrational modes favors adiabatic ET. Adiabatic ET requires an
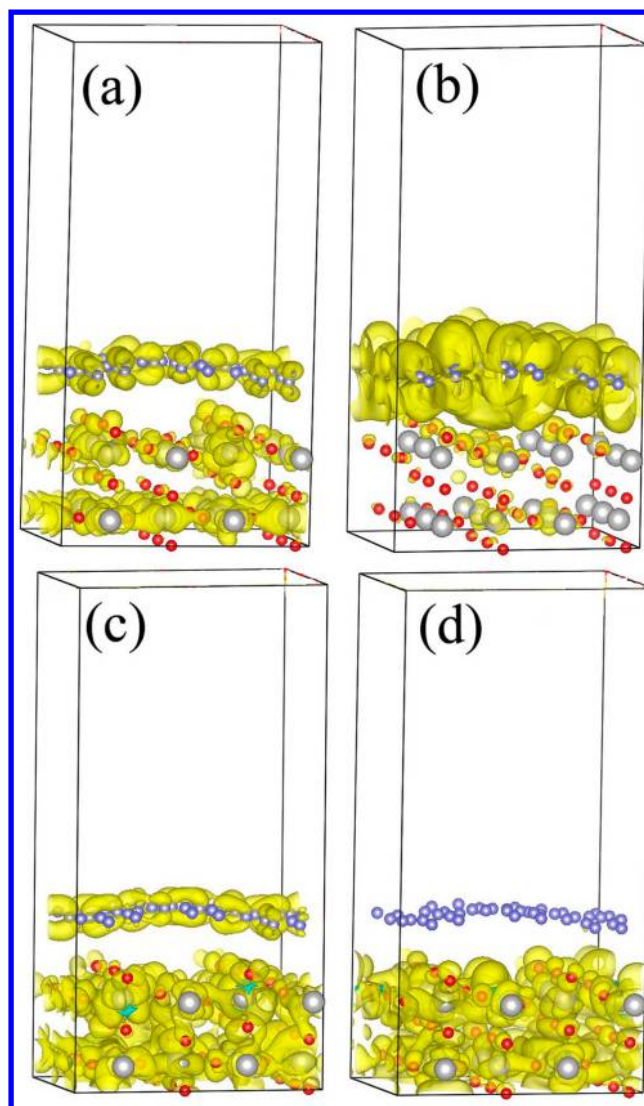
Figure 4. Charge densities of (a, b, c) different photoexcited electron donor states and (d) acceptor state. The photoexcited states exhibit different degrees of delocalization onto TiO$_2$, ranging from 20% for panel b to 45% for panel a and 60% for panel c. The energies of these states are shown in Figure 5a. The acceptor state (d) is localized entirely within TiO$_2$. The delocalization of the donor states into TiO$_2$ reflects the direct electron transfer mechanism, Figure 2, and is due to strong coupling between the two species.

activation energy, and therefore, exhibits exponential (Arrhenius) temperature dependence.[44] Similarly to direct ET, adiabatic electron injection can take place near the edge of TiO$_2$ CB, potentially avoiding energy losses to heat.[61] NA ET does not require strong donor–acceptor interactions and, therefore, occurs in a broader range of systems. Fast NA ET relies on a high density of acceptor states and, hence, cannot be efficient near the TiO$_2$ CB edge. The temperature dependence of NA ET arises[62] due to the nuclear velocity term in the NA coupling matrix element, eq 6. When the distance between the donor and acceptor species increases, for instance, because of a bridge, both direct and adiabatic ET stop. Then ET proceeds by the NA mechanism, showing exponential dependence on the bridge length. If the donor and acceptor species are very far from each other, ET becomes extremely slow, while energy transfer still can take place, in particular, by the Forster mechanism.[63]

2.3. Nonadiabatic Molecular Dynamics. The parametric dependence of the electron density on nuclear coordinates, eqs 1 and 3, determines the influence of vibrational motions on the

electronic evolution. The opposite effect, the back-reaction of electrons onto the nuclei, constitutes an essential part of the NAMD algorithm. NAMD also addresses the issue of electron−vibrational energy exchange. In particular in the present case, significant amounts of electronic energy are transferred to vibrations, and this effect is captured by the FSSH technique.[54]

Starting from eq 6, FSSH defines the probability of a transition from state k to state j within the time interval δt by[52]

$$g_{jk}(t, \delta t) = \max\left(0, \frac{b_{jk}\delta t}{a_{kj}(t)}\right) \tag{9}$$

where

$$a_{kj} = c_k(t)c_j(t)$$

and

$$b_{kj} = 2\hbar^{-1}\mathrm{Im}(a_{kj}\langle\tilde{\varphi}_k|H|\tilde{\varphi}_j\rangle) - 2\mathrm{Re}(a_{kj}\mathbf{d}_{kj})$$

If the calculated g_{jk} is negative, the hopping probability is set to zero; a hop from state j to state k can occur only when the electronic occupation of state j decreases and the occupation of state k increases. As shown in ref 54, FSSH maintains, to a good approximation, the detailed balance between transitions upward and downward in energy, ensuring that in the long-time limit the energy is fully and properly equilibrated between the electronic and vibrational subsystems. The current simulation uses a slightly simplified version of FSSH, as described in ref 59.

2.4. Simulation Details. Considering the previous experimental and theoretical studies of the hybrid graphene−TiO$_2$ systems,[64,65] we selected the stoichiometric rutile-TiO$_2$ (110) surface. The periodically repeated slab contained a 72-atom (3 × 2) surface composed of six atomic layers of TiO$_2$ with the bottom three layers frozen in the bulk configuration. The graphene sheet containing 42 carbon atoms was placed above the TiO$_2$ surface. The system was separated from its image along the surface normal by a vacuum region of 20 Å. The simulation cell is shown in Figure 3.

In order to test whether the reported results are robust with respect to the size of the simulation cell, we carried out two types of additional calculations. First, we added three atomic layers of TiO$_2$ to the simulation cell shown in Figure 3 and computed the band structure and a few representative values of the NA coupling. The band structure was very similar in both cases, and the NA couplings were of the same order of magnitude, allowing us to conclude that the six atomic layer representation of the TiO$_2$ surface is sufficient for the present purpose. Second, starting with the simulation cell shown in Figure 3, we increased the size of the vacuum region from 20 to 30 Å, computed the electronic energy levels and NA couplings, and performed a small number of NAMD runs. We obtained similar ET and energy relaxation time scales, indicating that the 20 Å vacuum region is sufficient to eliminate spurious interactions between the simulation cell images.

The electronic structure and adiabatic MD simulations were carried out with the Vienna *ab initio* simulation package (VASP).[66,67] Nonlocal exchange−correlation interactions were treated with the Perdew−Burke−Ernzerhof (PBE) functional[68] based on the generalized gradient approximation. We used the projector-augmented wave (PAW) method to represent the ionic cores and valence electrons.[69,70] In order to describe the electronic structure of TiO$_2$ more accurately owing to the presence of 3d electrons on Ti, we carried out DFT+U[71] calculations for geometry optimization and subsequent MD. The on-site $U = 6.0$ eV and $J = 0.5$ eV parameters were applied to the Ti 3d electrons.[72]

After relaxing the geometry at 0 K, we used velocity rescaling to bring the temperature of the hybrid graphene−TiO$_2$ system to 300 K, similar to the temperature in the experiment.[17] We then performed a 4 ps adiabatic MD simulation in the microcanonical ensemble with a 1 fs atomic time-step. The adiabatic state energies and NA couplings were calculated for each step of the MD run. Multiple configurations were harvested from the production run and used as initial configurations of the system at the time of photoexcitation. For each configuration in the hybrid graphene−TiO$_2$ system, the KS orbital corresponding to the PE state was chosen by selecting the adiabatic state with the largest optical transition dipole moment within the relevant energy range. An electron was promoted from the highest occupied orbital to the PE state orbital, and a NAMD run was initiated. The TDKS equations, eq 5, were propagated with the second-order differencing scheme[73] using an attosecond (10^{-3} fs) time step.

3. RESULTS AND DISCUSSION

The time-domain simulations of the photoinduced ET dynamics at the graphene−TiO$_2$ interface present a detailed real-time atomistic picture of ET, energy relaxation, and energy transfer processes at the interface. Nuclear motions play key roles in the electronic dynamics by modulating the electronic state energies, driving the system through donor−acceptor coupling regions, and producing electronic energy losses to heat. The ET process occurs from a PE state that is substantially delocalized onto the TiO$_2$ surface to begin with. While the adiabatic and NA ET mechanisms compete with each other, the NA mechanism dominates. ET that is faster than energy relaxation is a key desideratum in the improvement of the efficiency of solar-to-electricity conversion. The simulations demonstrate that this goal can be achieved in tightly coupled graphene−TiO$_2$ interfaces. Furthermore, in such scenarios, energy transfer is faster than energy relaxation, so that the energy in the TiO$_2$ lattice increases initially, even though the overall energy relaxes. In this section, we describe and analyze in detail these and related results of our NAMD simulations performed employing the TDKS-FSSH technique.[47,48]

3.1. Geometric and Electronic Structure of the Graphene−TiO$_2$ System. The interaction between graphene and the TiO$_2$ surface determines the rate and mechanisms of the ET process, as well as the efficiency of ET in competition with energy relaxation. The graphene−TiO$_2$ geometry and separation characterize the strength of the interfacial interaction. Figure 3 shows the top and side views of the system relaxed at 0 K (left panel) and a geometry from the MD run at 300 K (right panel). Comparing the zero- and finite-temperature geometries, we observe that the graphene sheet remains bound to the TiO$_2$ substrate at room temperature, even though the average separation increases from 2.617 to 3.211 Å. The graphene sheet is flat at 0 K, indicating that the π-electron system remains intact and that indeed the graphene−TiO$_2$ interaction is van der Waals rather than covalent, in agreement with the earlier calculations on the graphene−Ni(111)[74] and graphene−Pt(100) interfaces.[75]

As temperature increases, the TiO$_2$ structure changes little. More pronounced changes occur within the graphene sheet, Figure 3. Some of the six-atom rings become four- and eight-atom rings (top view at 300 K), and the whole sheet undergoes large-scale undulating motions (side view at 300 K). The oxygens terminating the TiO$_2$ surface tend to form bridge-like structures by positing themselves between and close to carbons. For instance, the two four-atom carbon rings in the bottom right corner of the top-view at 300 K are clustered around these oxygens. The bridging binding pattern is similar to that observed in ref 74. Calculated previously in graphene[76] and boron nitride[77] structures, dislocations of carbon atoms are caused by interactions with adatoms,[78,79] which behave similarly to bridging oxygens of the rutile TiO$_2$ (110) surface. Calculations show[74] that purely van der Waals interactions of graphene with ideal surfaces may be too weak to maintain

graphene-surface binding at room temperature. The rearrangements of carbon rings caused by interactions with the TiO_2 surface indicate that the graphene–TiO_2 binding occurs at room temperature in part due to chemical bonding.

The out-of-plane displacements of the carbon atoms (side view at 300 K in Figure 3) have a strong effect on the ET and energy relaxation dynamics, since they perturb the π-electron conjugation, raising and generally modulating the energies of graphene electronic states. In addition, the increasing graphene–TiO_2 separation serves to decrease the donor–acceptor coupling strength. The decrease has a strong effect on the rate of the NA ET, which is similar to tunneling and shows exponential dependence on the donor–acceptor separation. The low-frequency out-of-plane motion represents one type of vibration responsible for the electron–phonon coupling. In a realistic system, not limited by the size of the simulation cell, these motions should exhibit longer wavelengths and lower frequencies. High-frequency carbon–carbon stretching modes also contribute to the NA coupling, since they are fast and create large nuclear velocities, dR/dt, that enter the electron–phonon coupling matrix element, eq 6. The high-frequency motions are hard to detect by visualization of the MD trajectory, since they have small amplitude. The contribution of these modes to the ET dynamics becomes apparent in the analysis of the Fourier transforms of the electronic energy levels, presented below.

The electronic interaction between the electron donor and acceptor species mixes their states. Generally, the stronger is the interaction, the more significant is the mixing. Photoexcitation of an electron from a localized donor state into a state that exhibits a significant delocalization onto the acceptor constitutes the direct ET mechanism, Figure 2. In some cases,[39−41] direct ET is the primary ET mechanism. This is true if the excited state of the donor has a significantly higher energy than the acceptor state. In the present system, both donor and acceptor energy levels form continuous bands, the PE state is delocalized between graphene and TiO_2, and the direct mechanism is responsible for a part of the overall ET process.

The strength of the donor–acceptor coupling is directly reflected in the amount of mixing between the donor and acceptor orbitals. The mixing occurs due to interaction of the π-electron subsystem of the graphene sheet with the 3d-electrons of the under-coordinated Ti atoms of the surface. Figure 4a−c shows examples of PE states taken at different energies, Figure 5a. The examples illustrate a relatively broad range of donor–acceptor state mixing observed in the simulations. Figure 3a presents the situation in which the PE state density is distributed equally between the graphene sheet and the TiO_2 surface. About 45% of the PE electron is delocalized into TiO_2, indicating that the direct ET mechanism is responsible for nearly half of the overall injection process. The example of Figure 4b shows a PE state that is localized heavily on the graphene donor. Only a small amount of the PE electron density spills into the TiO_2 substrate. Figure 4c demonstrates the situation in which over 60% of the PE electron is already inside the TiO_2 substrate. As will be shown below, a larger delocalization of the PE state onto TiO_2 correlates with a shorter time scale for the transfer of the remaining electron density from the donor to the acceptor. For instance, the ET is faster for the initial condition shown in Figure 4c than that in Figure 4b. This is to be expected, since the strength of the electronic donor–acceptor coupling determines both the amount of state mixing and the ET rate.
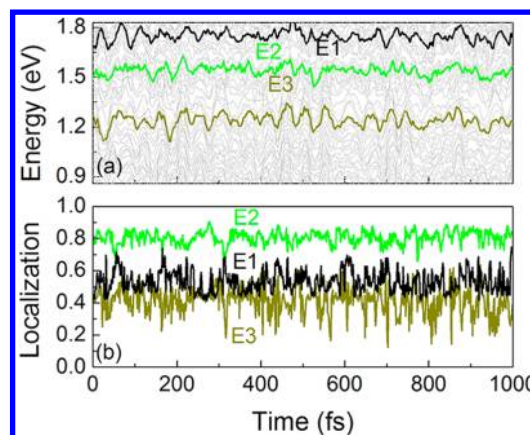
Figure 5. (a) Evolution of the energies of the photoexcited states E1, E2, and E3 (thick black, green, and brown lines) and TiO_2 conduction band states (thin gray lines). The spatial densities of E1, E2, and E3 are shown in Figure 4a−c, respectively. The energies fluctuate by about 0.1 eV, primarily as a result of graphene out-of-plane vibrational motions, Figure 2. (b) Evolution of the photoexcited state localizations on the graphene sheet. The localizations fluctuate mainly because of changes in the donor–acceptor coupling between graphene and TiO_2, induced by atomic motions. Stronger donor–acceptor coupling causes both larger state delocalization and its greater fluctuation, part b, for example, the localization of E3 on graphene is smaller and fluctuates more, compared with those of E1 and E2. There exists no obvious correlation between the photoexcited state energy and delocalization, compare parts a and b.
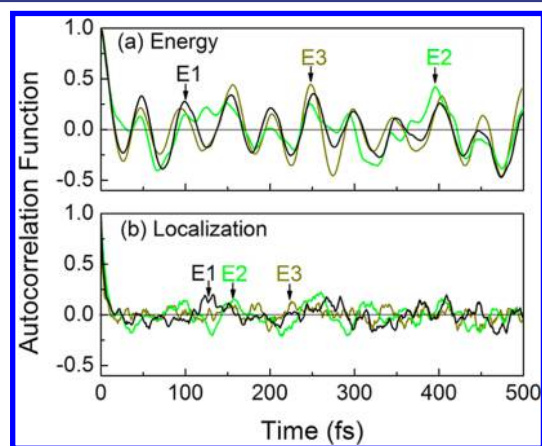
Figure 4d demonstrates that the electron acceptor state is localized entirely within the TiO_2 slab. Thus, the overall photoinduced ET process can be broken into two distinct steps. First, absorption of a photon promotes an electron from the ground electronic state of graphene into an excited state that is delocalized at the interface between graphene and TiO_2. Then, the electron moves from the interfacial state into bulk TiO_2, while at the same time losing energy to heat due to electron–vibrational interactions.

3.2. Nuclear Dynamics. Atomic motions contribute to the photoinduced ET dynamics in multiple ways. By distorting the equilibrium geometry of the system, they generate an ensemble of inhomogeneous initial conditions prior to the photoexcitation. During the ET dynamics, motions along the reaction coordinate drive the system over the transition state of adiabatic ET. At the same time, vibrations generate the NA coupling, eq 6, that induces transitions between electronic states and results in both NA ET and electron–vibrational energy relaxation.

Figure 5a shows the evolution of the energies of the three PE states, whose orbital densities are presented in Figure 4a−c. The states are identified within a narrow energy range to have the largest oscillator strength for the optical excitation from the ground state of graphene and to produce a smooth time dependence. The initial conditions for the photoinduced dynamics are sampled from these trajectories. The energy fluctuation of all three PE states is on the order of 100 meV. The inhomogeneous distribution of the PE state energy owing to thermal fluctuations is much smaller than the graphene excitation energy or the TiO_2 band gap; however, this has an obvious influence on the position of the donor state vis-à-vis the acceptor states. It can be seen in Figure 5a that the three PE states cross many states of the TiO_2 CB, which can lead to fast ET.

The evolution of the localization of the three PE states is shown in Figure 5b. Here, the y-axis represents the fraction of the PE state density on the graphene sheet. When the localization is high, the PE state is very similar to an excited state of isolated graphene. Conversely, when the localization is low, the PE state is a superposition of graphene and TiO$_2$ surface states. Closely related to the donor–acceptor coupling, the state localizations fluctuate along the trajectory around the average values that agree with the orbital densities shown in Figure 4. In particular, state E2 has the most localization on graphene, while state E3 has the least localization. While the relative order of state localizations remains constant over the 1 ps time scale shown in Figure 5b, the absolute localization values fluctuate significantly. For instance, the fraction of the E2 state density situated on graphene varies from 60% to 90%. The corresponding range for state E3 extends from 20% to 60%. These numbers reflect the contribution of the direct ET mechanism, Figure 2, to the overall ET process. The spread of the localization between graphene and the TiO$_2$ slab owes to the strong electronic coupling between them; in particular, the coupling of E3 and TiO$_2$ CB states is much stronger than the coupling of E1 and E2 with the TiO$_2$ states. In addition to the extent of direct ET, the strength of the donor–acceptor coupling determines the rate of the subsequent transfer of the electron density remaining on graphene into TiO$_2$.

Figure 5a,b illustrates the strong effect of vibrational motions on the PE energies and electron donor–acceptor coupling. In order to evaluate the randomness in the PE energy fluctuation and to identify the vibrational modes that couple to the electron dynamics, we computed the autocorrelation functions

Figure 7. Fourier transforms of (top) energy and (bottom) localization of the photoexcited states, Figure 5. The state energy couples most strongly to modes with frequencies between 400 and 800 cm^{-1}, corresponding to undulating motions of the graphene sheet, see Figure 3. State E2 also couples to the C–C stretching mode at 1500 cm^{-1}. The state localization, directly related to the graphene–TiO$_2$ donor–acceptor coupling, depends on a broader range of modes, including low-frequency modes of TiO$_2$ and graphene overtones around 2300 cm^{-1}.
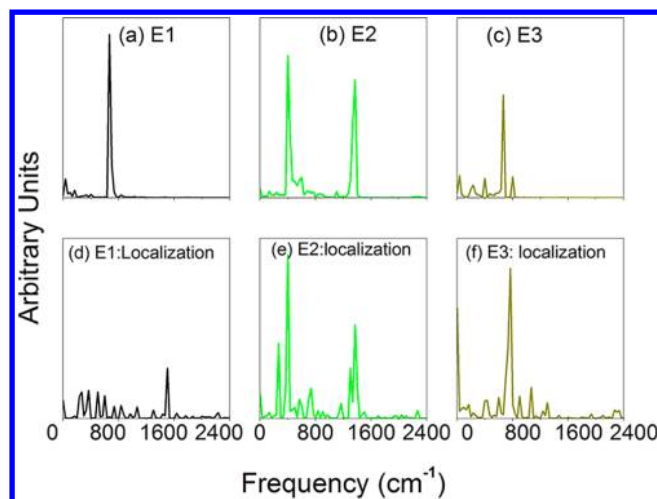

Figure 6. Autocorrelation functions of (a) energy and (b) localization of the three photoexcited states, Figure 5. The autocorrelations decay within 20 fs. The residual is significantly smaller for localization than energy, indicating that a broader range of vibrational modes affects the former than the latter. The localization is closely related to the donor–acceptor coupling, which is a more complex property of the wave function than the energy. The data show that in general more factors affect the coupling than the energy.

(ACFs) and Fourier transforms (FTs), Figures 6 and 7, respectively. The ACF of the PE state energy, $E(t)$, is defined as

$$C(t) = \frac{\langle E(t)E(0)\rangle}{\langle E^2\rangle}$$

It describes how the energy at a particular time depends on its value at earlier times. Generally, poorly correlated random

motion give ACFs that decrease rapidly from 1 to 0. Changes that are the result of well-correlated periodic vibrations lead to ACFs that oscillate between 1 and −1. The ACF of the PE state localization on graphene is defined similarly to the energy ACF.

The ACFs of the PE state energy and localization, parts a and b of Figure 6, decay rapidly at the early time. This initial decay can be well described by Gaussians with time scales of 15 and 30 fs for the energy and localization, respectively. The behavior of the two types of ACF differs dramatically at a later time. The energy ACF oscillates for a long time, with the dominant oscillation period of about 100 fs. The oscillation amplitude reaches 40% of the initial value for several hundred femtoseconds, indicating that the memory of the energy fluctuation extends into the picosecond regime. In contrast, the ACF of the PE state localization remains close to zero after the initial ultrafast decay. This result suggests that the electronic donor–acceptor coupling, determining the extent of the PE state delocalization between graphene and TiO$_2$, is much more sensitive to positions of the nuclei than the PE state energy and that the coupling fluctuates randomly on time scales longer than 10 fs.

Figure 7 presents the FTs of the PE state energy and localization (cf. Figure 5). The FTs support the conclusions obtained from the ACFs, Figure 6, that the localization couples to a broader spectrum of vibrational motions than the energy. This conclusion holds for all PE states considered here. The PE energy couples primarily to the high and intermediate frequency motions of the graphene sheet, including the C–C stretch at around 1500 cm^{-1} and carbon bond bending motions in the 400−800 cm^{-1} frequency range. Somewhat surprisingly, the signal from the low-frequency, large-scale, out-of-plane motions seen in Figure 3 is relatively weak. The high-frequency motions are harder to detect visually than the out-of-plane modes, emphasizing the importance of the FT analysis. The electronic donor–acceptor coupling, reflected in the delocalization of the PE state between graphene and TiO$_2$, is influenced

by a broad range of nuclear motions, including both high- and low-frequency modes. Low-frequency motions at the interface alter the donor–acceptor distance, thereby altering the coupling. Since the energy is computed by integrating over the wave function that is delocalized over large parts of the system, Figure 4, the effect of high-frequency local modes on the energy tends to average out during the integration. At the same time, small signals from overtones as high as 2300 cm^{-1} are seen in the localization FT, supporting the notion that the donor–acceptor interaction is sensitive to many factors.

Focusing on specific vibrational frequencies seen in the FT spectra of the PE energy and localization, we can identify a number of peaks in the 800–2000 cm^{-1} region, corresponding to various vibrational modes of the graphene Raman spectra.[80] The 1540 cm^{-1} peak is characteristic of the graphene G-band,[48,49] arising from C–C stretching motions. The peak at 1380 cm^{-1}, known as D band, is due to the breathing modes of sp^2 hybridized carbon rings.[80,81] The modes of the TiO$_2$ substrate appear at lower frequencies. The peak at 410 cm^{-1} is the fingerprint of rutile in a Raman spectrum.[82,83] The 690 cm^{-1} signal is also seen in the rutile TiO$_2$ Raman spectrum.[84] The TiO$_2$ modes contribute to the calculated FT spectra, because the PE state delocalizes onto TiO$_2$, Figures 4 and 5b.

3.3. Electron Injection Dynamics. The strong coupling between graphene and TiO$_2$ favors rapid electron injection, Figure 8. Both the contribution of direct ET by photoexcitation
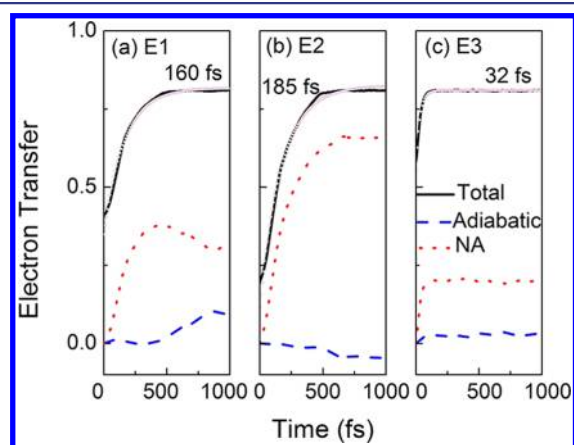
Figure 8. Average electron transfer dynamics for the E1, E2, and E3 photoexcited states shown in Figures 4 and 5. The solid black, dashed blue, and dotted red lines represent the total, adiabatic, and nonadiabatic electron transfer, respectively. The empty circles show the exponential fits, eq 12, of the total electron transfer data. The E1 and E2 time scales agree with experiment.[17] The E3 electron transfer is fast, because more than 50% of the photoexcited state is already localized on TiO$_2$. The nonadiabatic mechanism dominates, since electron transfer is accompanied by rapid electron-vibrational energy relaxation involving nonadiabatic transitions, Figure 9.

and the time needed to transfer the remaining fraction of the PE electron from graphene to TiO$_2$ correlate with the strength of the donor–acceptor interaction. The ET coordinate is defined by integrating the PE electron density over the region of the simulation cell occupied by the electron acceptor, that is, TiO$_2$, eq 7. The initial value of the ET coordinate shown in the y-axis of Figure 8 gives the contribution of the direct ET mechanism, Figure 2, to the overall ET process. The contribution is smallest for E2 and largest for E3. Correspondingly, the ET time is longest for E2 and shortest

for E3. The values for E1 fall in the middle. The data in Figure 8 were fitted with the following exponential function

$$y = y_0 + A \exp(-x/t) \tag{12}$$

Here, t is the ET time constant, and y_0 represents the contribution of the direct ET mechanism. Constant A reflects the sum of the amplitudes of the adiabatic and NA contributions to the overall ET. The asymptotic value of the ET coordinate is less than one due to finite size of the simulation cell and, in particular, of the TiO$_2$ representation, Figure 3. In the current simulation, the electron cannot escape into the TiO$_2$ bulk, and a fraction of the electron density remains on graphene. The calculated electron injection times agree well with the experimental value of 200 fs.[17] The agreement is best for E2, for which the PE state has the largest localization on graphene.

The evolution of the localization and occupations of the adiabatic states determines the mechanism of the ET dynamics, Figure 2 and eq 8. Adiabatic ET occurs by a change in the localization of the occupied state from graphene to TiO$_2$, taking place when the nuclear trajectory passes through a transition state along the reaction coordinate. NA ET involves a change in the state occupations during which the electron hops from a state localized on graphene to a state localized on TiO$_2$. NA ET can occur away from a transition state. In general, the adiabatic and NA ET mechanisms act simultaneously and compete with each other. The time scales and relative amounts of adiabatic and NA electron injection are calculated by separating the overall evolution of the ET coordinate into the contributions due to changes in the localization and occupation, respectively, according to eq 8.

The total, adiabatic, and NA ET are presented in Figure 8 by the black solid, blue dashed, and red dotted lines, respectively. Unexpectedly, the adiabatic ET contribution is very small, and the ET process is dominated entirely by NA ET. Our earlier studies of the photoinduced electron injection into TiO$_2$ from a number of systems, including molecular chromophores,[43–46] a water layer,[50] and a semiconductor quantum dot,[51] indicated that a strong donor–acceptor coupling leads to adiabatic ET. The coupling is weaker in the present system, since graphene forms only occasional chemical bonds with TiO$_2$. Nevertheless, analysis shows that the NA mechanism dominates over adiabatic ET not just because of the weaker coupling, but also and primarily due to the high density of donor and acceptor states. The donor–acceptor coupling is quite strong in the graphene–TiO$_2$ system. Since the energy levels of both graphene and TiO$_2$ form (quasi-)continuous manifolds, essentially every adiabatic eigenstate of the electronic Hamiltonian of the combined system is delocalized between graphene and the TiO$_2$ surface. The delocalization creates significant overlaps and large NA couplings between the states. A sequence of rapid NA transitions down the manifold of delocalized states, Figure 4a–c, and into the bulk-like states, Figure 4d, constitutes the primary ET mechanism at the graphene–TiO$_2$ interface.

3.4. Energy Relaxation and Transfer. The PE electron in the graphene–TiO$_2$ system relaxes rapidly down the dense (quasi-)continuous manifold of electronic states. One may be puzzled by the idea that a metal, such as graphene, can be used to harvest light for photovoltaic purposes.[19–22] Typically, the electrons and holes generated in a metal by light rapidly transfer the excess energy to heat and annihilate. In order to achieve the photovoltaic effect, the charge separation must be

14245

dx.doi.org/10.1021/ja3063953 | J. Am. Chem. Soc. 2012, 134, 14238−14248

faster than electron−vibrational energy losses. In this section, we explore the competition between the electron injection and the electron−vibrational energy relaxation. In addition, we investigate energy transfer, resulting from the combination of the above two processes.

Figure 9 presents the evolution of the PE electron energy for the three initial conditions considered previously. In each case,
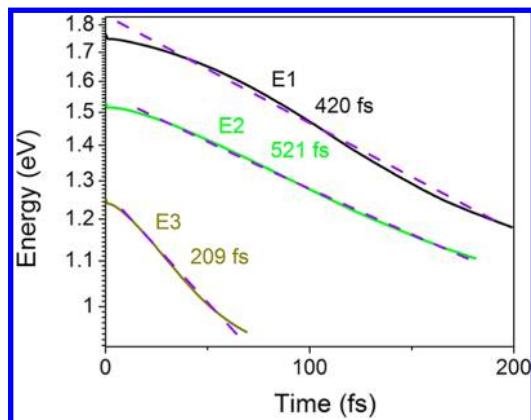
Figure 9. Semilogarithmic plot of energy relaxation on the three photoexcited states, Figures 3 and 4. The inverse of the slopes, shown as dashed lines, gives the relaxation time. In all cases, the energy relaxation is slower than the electron transfer, Figure 8, indicating that efficient charge separation can be obtained in the graphene−TiO$_2$ composites.

the energy is plotted on a semilogarithmic scale, and the data are fitted by eq 12. In the current fit, t is the energy relaxation time scale, y_0 is related to the initial energy, and the amplitude A is determined by the energy range included in the calculation. The semilogarithmic plot illustrates clearly that the initial part of the energy relaxation is not exponential, as commonly known with many other systems. Our simulations agree well with the experimental finding that the electronic energy relaxation in graphene takes place within a few hundred femtoseconds.[27,28] Comparison of the ET and energy relaxation times shown in Figures 8 and 9, respectively, proves that rapid and efficient ET is possible in the graphene−TiO$_2$ composite in spite of the energy losses. Consistently for all three initial conditions, ET is 3−5 times faster than energy relaxation. The energy relaxation time correlates with the ET time, indicating that larger graphene−TiO$_2$ coupling leads to faster relaxation. This is because the mixing between the graphene and TiO$_2$ state manifolds creates a single, dense set of states, all of which are strongly coupled by the NA interaction.

The combination of ET and energy relaxation creates conditions for the excitation energy transfer from graphene into TiO$_2$. This process is analyzed in Figure 10, which shows the distribution of the excess energy between the two subsystems. At time zero, the energy is distributed between graphene and TiO$_2$ according to the delocalization of the PE state. In cases E1 and E2, the PE state is localized primarily on graphene, see the initial data point in Figure 8. Therefore, graphene carries more excess energy than TiO$_2$, Figure 10. In contrast, the PE state E3 is more than 50% localized on TiO$_2$, Figure 8c. Hence, at time zero, TiO$_2$ already carries more excess energy than graphene in this case, Figure 10c. For all three initial conditions, the TiO$_2$ energy grows, even though the overall energy decreases, Figure 9. Thus, the energy transfer is faster than the energy relaxation. This qualitative conclusion is
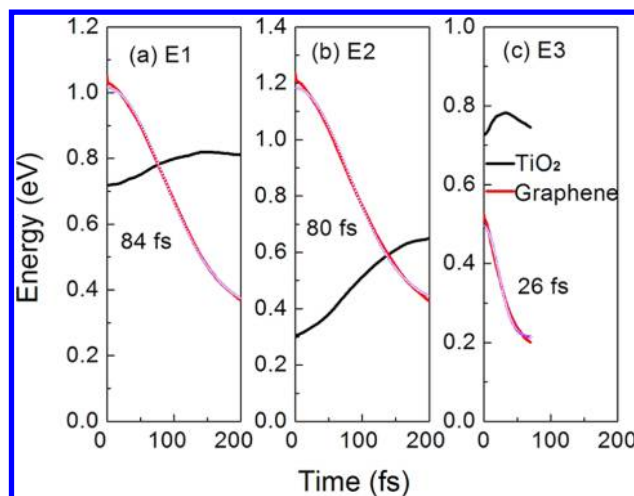
Figure 10. Energy transfer from graphene to TiO$_2$. Overall energy relaxation, Figure 9, is accompanied by faster energy transfer, as evidenced by transient heating of TiO$_2$.

confirmed by the Gaussian fits of the energy stored in graphene. The time scales obtained from these fits are reported in Figure 10.

The results discussed in sections 3.3 and 3.4 demonstrate that graphene−TiO$_2$ composites can provide high solar-to-electricity conversion efficiency because the ET process is more rapid than the energy relaxation.

4. CONCLUSIONS

The electronic structure and mechanisms of the photoinduced interfacial charge transfer, energy relaxation, and energy transfer have been investigated in a hybrid graphene−TiO$_2$ system in real time and at the atomistic level using a mixed quantum-classical approach that combines TD-DFT with NAMD. The simulations mimic directly the experimentally observed time-resolved electron transfer and energy relaxation processes and establish the mechanisms responsible for the movement of charge and energy through the system. The electron injection from graphene into TiO$_2$ occurs on an ultrafast time scale due to strong donor−acceptor coupling, favoring photoexcitation of states that are delocalized significantly between the two subsystems. The subsequent evolution occurs by rapid nonadiabatic transitions down the manifold of delocalized states, resulting in simultaneous ET, energy transfer and electron−vibrational energy relaxation.

The interaction between graphene and the bare rutile (110) surface of TiO$_2$ is noncovalent. Although the oxygen atoms of the surface can form additional chemical bonds, they do not disrupt the π-electron system of graphene. This remains true at both zero and ambient temperatures. Graphene moves away from the TiO$_2$ surface by about 0.6 Å at room temperature, primarily due to thermal excitation of long-range out-of-plane motions of graphene. These modes perturb the π-electron system, causing fluctuations of the graphene electronic energy levels. High-frequency carbon bond stretching and bending modes contribute to the PE electron dynamics by providing strong NA electron−vibrational coupling. The electronic donor−acceptor interaction is sensitive to a much broader range of atomic motions than the electronic energy. The former fluctuates randomly on time scale longer than 10 fs, while the latter exhibits coherent oscillations extending into the pico-second range.

The electron and energy transfer in graphene–TiO$_2$ composites can proceed in both directions, depending on the energy of the excited electron.[85–89] Once the electron relaxes to the bottom of the TiO$_2$ CB, it can transfer back onto graphene, since graphene has energy levels within the TiO$_2$ band gap. The back-transfer process competes with electron delocalization into bulk TiO$_2$ that is driven by entropy, related to the TiO$_2$ density of states. Our earlier studies[59] show that electron relaxation and delocalization inside TiO$_2$ proceed on similar time scales, and therefore, the details of ET from TiO$_2$ into graphene should be sensitive to TiO$_2$ bulk and surface traps,[88] dopants,[86,89] size of semiconductor particles,[85,87] and other factors, requiring multiscale investigation.

Since graphene is a metal, the photogenerated electrons and holes are expected to relax rapidly through the continuous manifold of states and annihilate. Therefore, one may wonder whether graphene can be used as a chromophore in photovoltaic devices. Our simulation shows that both ET and energy transfer from graphene to the TiO$_2$ surface are consistently faster than the relaxation, regardless of the excitation energy. This exciting finding rationalizes why graphene–TiO$_2$ solar cells have high direct light-to-current conversion efficiencies reported experimentally. Generated in our study, the detailed atomistic insights into the photoinduced electron–vibrational dynamics at the graphene–TiO$_2$ interface provide valuable contributions into a variety of fields, including photovoltaics, catalysis, electrolysis, and nanoscience.

■ AUTHOR INFORMATION

Corresponding Author
oleg.prezhdo@rochester.edu
Notes
The authors declare no competing financial interest.

■ ACKNOWLEDGMENTS

■ REFERENCES

(1) Hoffmann, M. R.; Martin, S. T.; Choi, W.; Bahnemann, D. W. *Chem. Rev.* **1995**, *95*, 69.

(2) Fujishima, A.; Honda, K. *Nature* **1972**, *238*, 37.

(3) Asahi, R.; Morikawa, T.; Ohwaki, T.; Aoki, K.; Taga, Y. *Science* **2001**, *293*, 269.

(4) Khan, S. U. M.; Al-Shahry, M.; Ingler, W. B. *Science* **2002**, *297*, 2243.

(5) Diebold, U. *Surf. Sci. Rep.* **2003**, *48*, 53.

(6) Carp, O.; Huisman, C. L.; Reller, A. *Prog. Solid State Chem.* **2004**, *32*, 33.

(7) Fujishima, A.; Zhang, X.; Tryk, D. A. *Surf. Sci. Rep.* **2008**, *63*, 515.

(8) Pan, L.; Zou, J.-J.; Zhang, X.; Wang, L. *J. Am. Chem. Soc.* **2011**, *133*, 10000.

(9) Wang, Y.; Li, L.; Yang, K.; Samuelson, L. A.; Kumar, J. *J. Am. Chem. Soc.* **2007**, *129*, 7238.

(10) Kongkanand, A.; Tvrdy, K.; Takechi, K.; Kuno, M.; Kamat, P. V. *J. Am. Chem. Soc.* **2008**, *130*, 4007.

(11) Wang, H.; Miyauchi, M.; Ishikawa, Y.; Pyatenko, A.; Koshizaki, N.; Li, Y.; Li, L.; Li, X.; Bando, Y.; Golberg, D. *J. Am. Chem. Soc.* **2011**, *133*, 19102.

(12) Zhang, L.; Diao, S.; Nie, Y.; Yan, K.; Liu, N.; Dai, B.; Xie, Q.; Reina, A.; Kong, J.; Liu, Z. *J. Am. Chem. Soc.* **2011**, *133*, 2706.

(13) Woan, K.; Pyrgiotakis, G.; Sigmund, W. *Adv. Mater.* **2009**, *21*, 2233.

(14) Kongkanand, A.; Martínez Domínguez, R.; Kamat, P. V. *Nano Lett.* **2007**, *7*, 676.

(15) Williams, G.; Seger, B.; Kamat, P. V. *ACS Nano* **2008**, *2*, 1487.

(16) Zhang, H.; Lv, X.; Li, Y.; Wang, Y.; Li, J. *ACS Nano* **2009**, *4*, 380.

(17) Manga, K. K.; Zhou, Y.; Yan, Y.; Loh, K. P. *Adv. Funct. Mater.* **2009**, *19*, 3638.

(18) Zhang, X.-Y.; Li, H.-P.; Cui, X.-L.; Lin, Y. *J. Mater. Chem.* **2010**, *20*, 2801.

(19) Tung, V. C.; Kim, J.; Cote, L. J.; Huang, J. *J. Am. Chem. Soc.* **2011**, *133*, 9262.

(20) Li, Q.; Guo, B.; Yu, J.; Ran, J.; Zhang, B.; Yan, H.; Gong, J. R. *J. Am. Chem. Soc.* **2011**, *133*, 10878.

(21) Iwase, A.; Ng, Y. H.; Ishiguro, Y.; Kudo, A.; Amal, R. *J. Am. Chem. Soc.* **2011**, *133*, 11054.

(22) Gupta, V.; Chaudhary, N.; Srivastava, R.; Sharma, G. D.; Bhardwaj, R.; Chand, S. *J. Am. Chem. Soc.* **2011**, *133*, 9960.

(23) Stoller, M. D.; Park, S.; Zhu, Y.; An, J.; Ruoff, R. S. *Nano Lett.* **2008**, *8*, 3498.

(24) Balandin, A. A.; Ghosh, S.; Bao, W.; Calizo, I.; Teweldebrhan, D.; Miao, F.; Lau, C. N. *Nano Lett.* **2008**, *8*, 902.

(25) Bolotin, K. I.; Sikes, K. J.; Jiang, Z.; Klima, M.; Fudenberg, G.; Hone, J.; Kim, P.; Stormer, H. L. *Solid State Commun.* **2008**, *146*, 351.

(26) Murphy, A. B. *Sol. Energy Mater. Sol. Cells* **2007**, *91*, 1326.

(27) Huang, L. B.; Hartland, G. V.; Chu, L. Q.; Luxmi; Feenstra, R. M.; Lian, C. X.; Tahy, K.; Xing, H. L. *Nano Lett.* **2010**, *10*, 1308.

(28) Gao, B.; Hartland, G.; Fang, T.; Kelly, M.; Jena, D.; Xing, H. L.; Huang, L. B. *Nano Lett.* **2011**, *11*, 3184.

(29) O'Regan, B.; Grätzel, M. *Nature* **1991**, *353*, 737.

(30) Grätzel, M. *Nature* **2001**, *414*, 338.

(31) Grätzel, M. *Inorg. Chem.* **2005**, *44*, 6841.

(32) Bisquert, J.; Cahen, D.; Hodes, G.; Rühle, S.; Zaban, A. *J. Phys. Chem. B* **2004**, *108*, 8106.

(33) Nazeeruddin, M. K.; Bessho, T.; Cevey, L.; Ito, S.; Klein, C.; De Angelis, F.; Fantacci, S.; Comte, P.; Liska, P.; Imai, H.; Grätzel, M. *J. Photochem. Photobiol., A* **2007**, *185*, 331.

(34) Asbury, J. B.; Hao, E.; Wang, Y.; Ghosh, H. N.; Lian, T. *J. Phys. Chem. B* **2001**, *105*, 4545.

(35) Huber, R.; Moser, J.-E.; Grätzel, M.; Wachtveitl, J. *J. Phys. Chem. B* **2002**, *106*, 6494.

(36) Zhu, X. Y. *J. Phys. Chem. B* **2004**, *108*, 8778.

(37) Schwarz, O.; van Loyen, D.; Jockusch, S.; J. Turro, N.; Dürr, H. *J. Photochem. Photobiol., A* **2000**, *132*, 91.

(38) Asbury, J. B.; Ellingson, R. J.; Ghosh, H. N.; Ferrere, S.; Nozik, A. J.; Lian, T. *J. Phys. Chem. B* **1999**, *103*, 3110.

(39) Rego, L. G. C.; Batista, V. S. *J. Am. Chem. Soc.* **2003**, *125*, 7989.

(40) Abuabara, S. G.; Rego, L. G. C.; Batista, V. S. *J. Am. Chem. Soc.* **2005**, *127*, 18234.

(41) Kondov, I.; Wang, H. B.; Thoss, M. *Int. J. Quantum Chem.* **2006**, *106*, 1291.

(42) Li, J. R.; Kondov, I.; Wang, H. B.; Thoss, M. *J. Phys. Chem. C* **2010**, *114*, 18481.

(43) Duncan, W. R.; Stier, W. M.; Prezhdo, O. V. *J. Am. Chem. Soc.* **2005**, *127*, 7941.

(44) Duncan, W. R.; Prezhdo, O. V. *J. Am. Chem. Soc.* **2008**, *130*, 9756.

(45) Prezhdo, O. V.; Duncan, W. R.; Prezhdo, V. V. *Acc. Chem. Res.* **2008**, *41*, 339.

(46) Duncan, W. R.; Prezhdo, O. V. *Annu. Rev. Phys. Chem.* **2007**, *58*, 143.

(47) Craig, C. F.; Duncan, W. R.; Prezhdo, O. V. *Phys. Rev. Lett.* **2005**, *95*, No. 163001.

(48) Fischer, S. A.; Habenicht, B. F.; Madrid, A. B.; Duncan, W. R.; Prezhdo, O. V. *J. Chem. Phys.* **2011**, *134*, No. 024102.

(49) Habenicht, B. F.; Prezhdo, O. V. *Phys. Rev. Lett.* **2008**, *100*, No. 197402.

(50) Fischer, S. A.; Duncan, W. R.; Prezhdo, O. V. *J. Am. Chem. Soc.* **2009**, *131*, 15483.

(51) Long, R.; Prezhdo, O. V. *J. Am. Chem. Soc.* **2011**, *133*, 19240.

(52) Tully, J. C. *J. Chem. Phys.* **1990**, *93*, 1061.

(53) Hammes-Schiffer, S.; Tully, J. C. *J. Chem. Phys.* **1994**, *101*, 4657.

(54) Parandekar, P. V.; Tully, J. C. *J. Chem. Phys.* **2005**, *122*, No. 094102.

(55) Li, X.; Tully, J. C.; Schlegel, H. B.; Frisch, M. J. *J. Chem. Phys.* **2005**, *123*, No. 084106.

(56) Baer, R.; Neuhauser, D. *J. Chem. Phys.* **2004**, *121*, 9803.

(57) Tretiak, S.; Igumenshchev, K.; Chernyak, V. *Phys. Rev. B* **2005**, *71*, No. 033201.

(58) Kohn, W.; Sham, L. J. *Phys. Rev.* **1965**, *140*, A1133.

(59) Duncan, W. R.; Craig, C. F.; Prezhdo, O. V. *J. Am. Chem. Soc.* **2007**, *129*, 8528.

(60) Isborn, C. M.; Li, X. S.; Tully, J. C. *J. Chem. Phys.* **2007**, *126*, No. 134307.

(61) Stier, W.; Duncan, W. R.; Prezhdo, O. V. *Adv. Mater.* **2004**, *16*, 240.

(62) Bao, H.; Habenicht, B. F.; Prezhdo, O. V.; Ruan, X. L. *Phys. Rev. B* **2009**, *79*, No. 235306.

(63) Algar, W. R.; Wegner, D.; Huston, A. L.; Blanco-Canosa, J. B.; Stewart, M. H.; Armstrong, A.; Dawson, P. E.; Hildebrandt, N.; Medintz, I. L. *J. Am. Chem. Soc.* **2012**, *134*, 1876.

(64) Du, A.; Smith, S. C. *J. Phys. Chem. Lett.* **2010**, *2*, 73.

(65) Du, A.; Ng, Y. H.; Bell, N. J.; Zhu, Z.; Amal, R.; Smith, S. C. *J. Phys. Chem. Lett.* **2011**, *2*, 894.

(66) Kresse, G.; Furthmüller, J. *Phys. Rev. B* **1996**, *54*, 11169.

(67) Kresse, G.; Hafner, J. *Phys. Rev. B* **1993**, *47*, 558.

(68) Perdew, J. P.; Burke, K.; Ernzerhof, M. *Phys. Rev. Lett.* **1996**, *77*, 3865.

(69) Blöchl, P. E. *Phys. Rev. B* **1994**, *50*, 17953.

(70) Kresse, G.; Joubert, D. *Phys. Rev. B* **1999**, *59*, 1758.

(71) Dudarev, S. L.; Botton, G. A.; Savrasov, S. Y.; Humphreys, C. J.; Sutton, A. P. *Phys. Rev. B* **1998**, *57*, 1505.

(72) Calzado, C. J.; Hernández, N. C.; Sanz, J. F. *Phys. Rev. B* **2008**, *77*, No. 045118.

(73) Leforestier, C.; Bisseling, R. H.; Cerjan, C.; Feit, M. D.; Friesner, R.; Guldberg, A.; Hammerich, A.; Jolicard, G.; Karrlein, W.; Meyer, H. D.; Lipkin, N.; Roncero, O.; Kosloff, R. *J. Comput. Phys.* **1991**, *94*, 59.

(74) Fuentes-Cabrera, M.; Baskes, M. I.; Melechko, A. V.; Simpson, M. L. *Phys. Rev. B* **2008**, *77*, No. 035405.

(75) Nilsson, L.; Andersen, M.; Bjerre, J.; Balog, R.; Hammer, B.; Hornekaer, L.; Stensgaard, I. *Surf. Sci.* **2012**, *606*, 464.

(76) Cockayne, E.; Rutter, G. M.; Guisinger, N. P.; Crain, J. N.; First, P. N.; Stroscio, J. A. *Phys. Rev. B* **2011**, *83*, No. 195425.

(77) Liu, Y.; Zou, X.; Yakobson, B. I. *ACS Nano* **2012**, DOI: 10.1021/nn302099q.

(78) Rutter, G. M.; Crain, J. N.; Guisinger, N. P.; Li, T.; First, P. N.; Stroscio, J. A. *Science* **2007**, *317*, 219.

(79) Cretu, O.; Krasheninnikov, A. V.; Rodriguez-Manzo, J. A.; Sun, L. T.; Nieminen, R. M.; Banhart, F. *Phys. Rev. Lett.* **2010**, *105*, No. 196102.

(80) Casiraghi, C.; Hartschuh, A.; Qian, H.; Piscanec, S.; Georgi, C.; Fasoli, A.; Novoselov, K. S.; Basko, D. M.; Ferrari, A. C. *Nano Lett.* **2009**, *9*, 1433.

(81) Ferrari, A. C.; Robertson, J. *Phys. Rev. B* **2000**, *61*, 14095.

(82) Mazza, T.; Barborini, E.; Piseri, P.; Milani, P.; Cattaneo, D.; Li Bassi, A.; Bottani, C. E.; Ducati, C. *Phys. Rev. B* **2007**, *75*, No. 045416.

(83) Swamy, V. *Phys. Rev. B* **2008**, *77*, No. 195414.

(84) Guo, X.-Y.; Xu, D.-P.; Ding, Z.-H.; Su, W.-H. *Chin. Phys. Lett.* **2006**, *23*, 1645.

(85) Kamat, P. V. *J. Phys. Chem. Lett.* **2010**, *1*, 520.

(86) Jung, N.; Kim, N.; Jockusch, S.; Turro, N. J.; Kim, P.; Brus, L. *Nano Lett.* **2009**, *9*, 4133.

(87) Li, Q.; Guo, B. D.; Yu, J. G.; Ran, J. R.; Zhang, B. H.; Yan, H. J.; Gong, J. R. *J. Am. Chem. Soc.* **2011**, *133*, 10878.

(88) Zhang, L. M.; Diao, S. O.; Nie, Y. F.; Yan, K.; Liu, N.; Dai, B. Y.; Xie, Q.; Reina, A.; Kong, J.; Liu, Z. F. *J. Am. Chem. Soc.* **2011**, *133*, 2706.

(89) Crowther, A. C.; Ghassaei, A.; Jung, N.; Brus, L. E. *ACS Nano* **2012**, *6*, 1865.